## PAPER

# Adsorption, photodegradation and antibacterial study of graphene–Fe₃O₄ nanocomposite for multipurpose water purification application†

Chella Santhosh,[a] Pratap Kollu,‡*[b] Sejal Doshi,[c] Madhulika Sharma,[c] Dhirendra Bahadur,*[c] Mudaliar T. Vanchinathan,[a] P. Saravanan,[d] Byeong-Su Kim[e] and Andrews Nirmala Grace*[a]

Graphene–Fe₃O₄ (G–Fe₃O₄) composite was prepared from graphene oxide (GO) and FeCl₃·6H₂O by a one-step solvothermal route. The as-prepared composite was characterized by field-emission scanning electron microscopy, transmission electron microscopy, dynamic light scattering and X-ray powder diffraction. SEM analysis shows the presence of Fe₃O₄ spheres with size ranging between 200 and 250 nm, which are distributed and firmly anchored onto the wrinkled graphene layers with a high density. The resulting G–Fe₃O₄ composite shows extraordinary adsorption capacity and fast adsorption rates for the removal of Pb metal ions and organic dyes from aqueous solution. The adsorption isotherm and thermodynamics were investigated in detail, and the results show that the adsorption data was best fitted with the Langmuir adsorption isotherm model. From the thermodynamics investigation, it was found that the adsorption process is spontaneous and endothermic in nature. Thus, the as-prepared composite can be effectively utilized for the removal of various heavy metal ions and organic dyes. Simultaneously, the photodegradation of methylene blue was studied, and the recycling degradation capacity of dye by G–Fe₃O₄ was analyzed up to 5 cycles, which remained consistent up to ∼97% degradation of the methylene blue dye. Although iron oxide has an affinity towards bacterial cells, its composite with graphene still show antibacterial property. Almost 99.56% cells were viable when treated with Fe₃O₄ nanoparticle, whereas with the composite barely 3% cells survived. Later, the release of ROS was also investigated by membrane and oxidative stress assay. Total protein degradation was analyzed to confirm the effect of the G–Fe₃O₄ composite on *E. coli* cells.

## Introduction

Water pollution resulting from biotic and abiotic pollutants has been a major environmental threat attributable to both existing and emerging industries. Heavy metals and dyes beyond the permissible limits directly cause toxicity to humans and other living organisms. Metal ions, such as Cd(II) and Pb(II) have been reported to immobilize the enzymes in some plants and can also cause energy deficiency in the transmission of nerve impulses in humans.[1,2] Hence, it has become immediately necessary to prevent water pollution caused by microbes as well as by heavy metals and dyes. Most purification methods suffer from some drawbacks such as high capital and operational costs or disposal of residual metal sludge, and hence are not suitable for small scale industries.[3] In addition, these methods are not very efficient at low concentrations in the range 1–100 mg L$^{-1}$.[4,5] Silver has become the basis for antibacterial activity; however, because silver is expensive and leaches into the environment, the focus has shifted to the exploration of inexpensive materials for antibacterial activity.

Adsorption is one of the promising processes for the removal of heavy metal ions from water. Some of the adsorbent materials for heavy metal ion removal are activated carbon (powder or granular) and CNTs, *etc.*,[6–8] for the removal of Pb, cadmium and other heavy metal ions. However, the cost of adsorbent becomes relatively high when pure sorbents are used. Photodegradation of dye has been a successful method for the

[a]Centre for Nanotechnology Research, VIT University, Vellore 632014, India. E-mail: anirmalagladys@gmail.com; anirmalagrace@vit.ac.in; Tel: +919791322311

[b]DST-INSPIRE Faculty, Department of Metallurgical Engineering and Materials Science, Indian Institute of Technology Bombay, Mumbai 400076, India

[c]Department of Metallurgical Engineering and Materials Science, Indian Institute of Technology Bombay, Mumbai 400076, India. E-mail: dhirenb@iitb.ac.in

[d]Defence Metallurgical Research Laboratory, Hyderabad 500 058, India

[e]Department of Chemistry and Department of Energy Engineering, Ulsan National Institute of Science and Technology (UNIST), UNIST-gil 50, Ulsan 689-798, Korea

† Electronic supplementary information (ESI) available. See DOI: 10.1039/c4ra02913e

‡ Current address: Thin Film Magnetism group, Cavendish Laboratory, Department of Physics, University of Cambridge, Cambridge CB3 0HE, UK. Email: pk419@cam.ac.uk

eradication of dyes from effluent water, which further helps in water purification.

Graphene and $Fe_3O_4$ (ref. 9 and 10) individually have been reported for their filtration and purification activity. For standalone use they can be used as water-purifying materials, thus it was considered to combine them as a composite and efficiently use them as a nanomaterial for water purification. Graphene is a single layer of carbon densely packed in a honeycomb crystal lattice structure. In comparison with other carbonaceous material, it has drawn much attention since its discovery due to its unique electronic and mechanical properties.[11,12] Its remarkable properties, such as large surface area ($2630 \ m^2 \ g^{-1}$), good chemical stability, flat structure, imply that it can be used as an excellent adsorbent.[13–16] Its basal plane structure allows for strong $\pi$–$\pi$ interactions, assigned to the $\pi$–$\pi$ stacking between aromatic dyes and the $\pi$-conjugation regions of the graphene layers.[17]This property of graphene would serve as a good adsorbent for removing pollutants such as metal ions, dyes, and biological materials. However, graphene sheets usually suffer from serious agglomeration and restacking due to their $\pi$–$\pi$ interactions between neighbouring sheets, leading to a significant loss of effective surface area and lower adsorption capacity.[18,19] To overcome such difficulties, magnetic adsorbents have emerged as new generation materials for environmental application. The advantage of such materials is their ability to effect magnetic separation by applying an external magnetic field to extract the adsorbent material from the suspension.[20,21]

Compared with traditional methods, such as filtration, centrifugation and gravitational separation, magnetic separation requires less energy and better separation can be achieved. Therefore, the synthesis of graphene with covalently attached $Fe_3O_4$ offers an effective approach to overcome the separation problem associated with graphene. At the same time, the attachment of $Fe_3O_4$ with graphene provides a decrease in the possibility of serious agglomeration. In this regard, the current work is focused on the synthesis of G–$Fe_3O_4$ composites by a solvothermal route. Further, the as-prepared composites were tested for adsorption properties towards Pb ions and the photodegradation of methylene blue. To better understand its antimicrobial mechanism, we compared the antibacterial activity of graphene and G–$Fe_3O_4$ towards a bacterial model, *Escherichia coli*. Under similar concentration and incubation conditions, G–$Fe_3O_4$ dispersion shows the highest antibacterial activity. ROS[22] and protein degradation were responsible for bacterial cell wall rupture.

# Experimental

## Materials

All chemicals were analytical grade, purchased from Sigma Aldrich and used as received without purification. Graphite powder, hydrogen peroxide (30 wt%), sodium nitrate (98%), sulphuric acid (98 wt%), potassium permanganate, $Pb(NO_3)_2$, $FeCl_3 \cdot 6H_2O$ and sodium acetate (NaAc) were purchased from SD-Fine and used as received.

## Preparation of graphene oxide

Graphene oxide (GO) was prepared from natural graphite powder by the modified Hummers method.[23] In a typical synthesis, 1 g of graphite was added to 23 mL of 98% $H_2SO_4$, followed by stirring at room temperature over a period of 24 h. Then, 100 mg of $NaNO_3$ was added to the mixture, stirred for 30 min and then maintained below 5 °C in an ice bath. Finally, 3 g of $KMnO_4$ was added slowly into the mixture. Afterwards, the mixture was heated to 35–40 °C with continuous stirring for 30 min. Then, 46 mL of water was added to the abovementioned mixture and mixed well for 25 min. Finally, 140 mL of water and 10 mL of 30% $H_2O_2$ were added to the mixture to stop the reaction. Unreacted graphite in the resulting mixture was removed by centrifugation and the resulting mixture was dried at 60 °C in a vacuum oven. The as-synthesized GO was dispersed into individual sheets in distilled water at a concentration of 0.5 mg $mL^{-1}$ with the help of ultrasound for further use.

## Synthesis of G-$Fe_3O_4$nanocomposites

The as-prepared GO was used as a precursor for the preparation of G–$Fe_3O_4$ composites by a one-step solvothermal method. In a typical synthesis, the as-prepared GO (0.5 g) was exfoliated by ultrasonication in 80 mL of ethylene glycol for more than 3 h. 1.6 g $FeCl_3 \cdot 6H_2O$ and 3.2 g NaAc were then dissolved in GO/EG solution at ambient temperature. After stirring for about 30 min, the solution was transferred to a 100 mL teflon-lined stainless-steel autoclave and maintained at 200 °C for 6 h, followed by naturally cooling to ambient temperature. The black precipitate was centrifuged, washed with ethanol several times and finally dried at 60 °C in a vacuum oven.

## Characterization

The particle size and morphology of the material was studied by FE-Scanning Electron Microscopy (FE-SEM) (HITACHI SU6600 SEM). The phase and crystallographic structure were identified by X-ray diffraction (XRD; Philips X'Pert Pro, Cu-K$\alpha$: $\lambda = 0.1540598$ nm). The adsorbed metal ion concentration was examined by an atomic adsorption spectrophotometer (Perkin-Elmer Analyst 240). Thermogravimetric analysis (TGA) of the samples was performed on an SDT Q600 (TA Instruments, Korea) with a heating rate of 5 °C $min^{-1}$ from 0° to 1000 °C. The G–$Fe_3O_4$ samples were characterized with a high resolution transmission electron microscope (HR-TEM) JEOL-2000EX operated at 120 kV. Dynamic light scattering measurements were performed using a Beckman Coulter Delsa™ Nano instrument.

## Analytical measurement

For analytical studies, analytical grade lead nitrate was used to prepare a stock solution containing 1000 mg $L^{-1}$ of $Pb(NO_3)_2$, which was further diluted with double-distilled deionized water to the required ionic concentration. Adsorption thermodynamic experiments were conducted in a 100 mL glass flask containing 25 mg of adsorbent and 100 mL of Pb ion solution at varying concentrations (10–50 mg $L^{-1}$) and pH 5. The samples were

then placed in an orbital shaker for continuous stirring at 250 rpm for different durations and at selected temperatures (300, 310, and 320 K). After a certain time, the suspension was filtered using 0.22 μm cellulose nitrate membrane, and the filtrates were immediately examined using atomic adsorption spectrophotometry (AAS) to measure the ion concentration. The difference between the initial and the equilibrium ion concentration gave the amount of ion adsorbed to the G–Fe$_3$O$_4$ surfaces.

## Batch mode adsorption

The effects of experimental parameters, such as initial concentration (10–50 mg L$^{-1}$), pH (3–8), and temperature, were studied in a batch mode of adsorption for specific contact times (0–180 min). To determine the effect of each parameter, the other parameters were maintained constant. Pb solution was prepared by dissolving Pb(NO$_3$)$_2$ in double distilled water and used as the stock solution. Then, the solutions were diluted to the required concentration for the experimental study. The pH of the solution was adjusted using 0.1 M HCl or 0.1 M NaOH. For contact time measurements, 100 mL of Pb ion solution containing 10 mg L$^{-1}$ of an initial ion concentration at pH 5 was put into a 250 mL conical flask with a fixed amount of adsorbent (25 mg L$^{-1}$) and agitated in an orbital shaker at 250 rpm and 310 K. At various intervals, the adsorbent were separated from the samples by filtering, and the filtrates were analyzed by AAS to determine the concentration of each ion in the solution.[24] The adsorption percentage of a metal ion was calculated as follows:

$$\text{Adsorption } (\%) = \frac{C_i - C_f}{C_i} \times 100 \qquad (1)$$

where $C_i$ and $C_f$ are the initial and final metal ion concentration (after contact with adsorbents), respectively.

## Photodegradation activity of G-Fe$_3$O$_4$

The photodegradation activity of the as-prepared G–Fe$_3$O$_4$ was evaluated by the photodegradation of methylene blue dye using 60 W of a visible light CFL lamp. For the degradation of dye, 0.2 g L$^{-1}$ of photocatalyst was added to 100 mL of methylene blue dye (10 mg L$^{-1}$) aqueous solution. 1 mL of 30% H$_2$O$_2$ was added to the reaction mixture at the beginning of light irradiation. About 1 mL of aliquot was withdrawn at a given irradiation time and then magnetically separated to remove the catalyst. In the case of bare graphene nanosheets, the suspension was separated by centrifuging at 3000 rpm. The concentration of the remaining dye was determined by measuring the absorbance of solutions at 664 nm by UV-vis spectroscopy.

## Biocompatibility of G-Fe$_3$O$_4$

Sulforhodamine-B (SRB) assay was performed to evaluate the biocompatibility of G–Fe$_3$O$_4$ with normal mouse fibroblast cells (L929). Although iron oxide nanoparticles have been well-established as biocompatible nanomaterials, it is essential to evaluate the toxic effect of G–Fe$_3$O$_4$ on cell proliferation and morphology of L929 cells because of the presence of graphene. It is important to test the toxic effect of functional material

towards a living system. The cells were seeded into 96-well plates at a density of $1 \times 10^4$ cells per well and incubated for 24 h in a 5% CO$_2$ environment. Then, 200 μL of different concentrations of the dispersed suspension of G–Fe$_3$O$_4$ (2.0, 1.0, 0.5, 0.25, 0.125, 0.625, and 0.3125 mg mL$^{-1}$) in DMEM growth medium were added to the cells and incubated for another 24 h at 37 °C and 5% CO$_2$ environment. Thereafter, the cells were gently washed with phosphate buffer saline (PBS; pH 7.3) and processed for SRB assay to determine the viable cell population. Non-treated cells were used as control for the experiments. The cells were then fixed with 10% trichloroacetic acid solution by incubating at 4 °C for 1 h. This was followed by gentle washing of cells with water and then staining with 0.4% SRB dissolved in 1% acetic acid and then incubating in the dark. The cell-bound dye was then extracted with 200 μL of 10 mM Tris buffer solution (pH 10.5), and its optical density was measured using a multiwall plate reader at 560 nm. The viable cell population was calculated using the following formula:

$$\% \text{ cell viablity} = \frac{\text{Absorbance of treated cells}}{\text{Absorbance of control cells}} \times 100$$

## Antibacterial activity of G-Fe$_3$O$_4$

*E. coli* were procured from K.C. College, Mumbai, India. The cultures were initially isolated from patients infected with water-borne disease. This culture has been sub-cultured for the last 20 years and hence is assumed to have very low virulence. Nutrient broth media was procured from HiMedia. All the chemicals were purchased from Sigma-Aldrich and used without further purification.

# Results and discussion

## Structural and morphological analysis

The phase composition and structures of G–Fe$_3$O$_4$ nanocomposites were examined using X-ray powder diffraction and the corresponding pattern is shown in Fig. S1.† In the pattern of GO (Fig. S1a†), a diffraction peak at 11.08° is observed, which corresponds to the (001) plane of graphene oxide structure. In Fig. S1b,† natural graphite shows diffraction peaks at 26.4°, 44.3° and 54.5° corresponding to the hexagonal lattice of the (002), (101) and (004) planes, respectively. The major peak is at 26.4°, which corresponds to a basal spacing of $d_{002} = 3.38$ Å. The typical process is the reduction of GO to graphene during the solvothermal process. After reduction, the peak at 11° completely disappeared and a weak hump (*) could be observed in Fig. S1(c).† In Fig. S1c,† G–Fe$_3$O$_4$ composite with diffraction peaks at 2θ values of 30.6°, 36.1°, 43.7°, 57.6°, 63.1° and 74.7° correspond to (220), (222), (400), (511), (440) and (533) planes of Fe$_3$O$_4$, respectively. This matches with the standard JCPDS no. 65-3107. The results indicate the existence of Fe$_3$O$_4$ in the composite material and clearly show the reduction of GO peak in the composite material. The disappearance of the peak at 2θ = 11° clearly indicated that GO was reduced to graphene. The absence of a sharp peak at 26° indicates that it is not graphite but should be graphene. The peak at 2θ = 26° pertaining to

graphene is not as intense because it is in the form of a composite and the $Fe_3O_4$ phase dominates the graphene layers. The graphene peak was not predominant because the stacking of graphene sheets in $G–Fe_3O_4$ was disordered and exfoliated to a large extent.[25,26]

## Morphological characterization of G-Fe$_3$O$_4$

Fig. 1 shows the surface morphology of $G–Fe_3O_4$ at different magnifications. The TEM images of $G–Fe_3O_4$ reveal that the product consists of a large quantity of $Fe_3O_4$ spheres with sizes ranging from 200 to 250 nm. After combination with graphene to form a $G–Fe_3O_4$ composite, the $Fe_3O_4$ spheres are decorated and firmly anchored on the wrinkled graphene layers with a high density, as shown in Fig. 1. Note that the pleated structure of graphene may favour the hindrance of the $Fe_3O_4$ spheres from agglomeration and enable their good distribution on graphene, whereas the $Fe_3O_4$ spheres serve as a stabilizer to separate graphene sheets against aggregation. In addition, the $Fe_3O_4$ spheres are observed to be porous in nature, which will further help in the adsorption process.

Further, dynamic light scattering measurements (DLS) were recorded, and the results showed that the nanoparticles are monodispersed (Fig. S2a†). The hydrodynamic sizes of the particles were found to be around 500 nm. In general, the hydrodynamic diameter takes into consideration factors such as solvation and other effects, and hence will be generally higher than that measured by other methods.[27] The sizes of the particles were further confirmed by SEM analysis, which showed the dispersion of $Fe_3O_4$ particles on graphene sheets (Fig. S2b†).

## TGA–DTA/BET analysis

Fig. S3† shows the TGA curve of the as-prepared $G–Fe_3O_4$ composite with a minor weight loss from 50 °C to 100 °C (∼10%) and major weight loss from 270 °C to 450 °C (∼40%). After this, no weight loss was obtained up to 1000 °C. A minor

weight loss was observed due to adsorbed water and loss of moisture in the as-prepared material. A major weight loss was due to graphene and $Fe_3O_4$ composite. Apparently, in DTA curve, two main exothermic peaks were obtained at 290 °C and 450 °C, which relate to the thermal decomposition of ferrites along with carbon.

The $N_2$ adsorption–desorption isotherm was used to determine the porous capacity of graphene–$Fe_3O_4$ (Fig. S4a†). According to IUPAC (International Union of Pure and Applied Chemistry) classification, the isotherms show typical type IV and type H3 hysteresis loop. This behaviour indicates the predominance of mesopores. The mesoporous nature is also evident from the sharp increment in adsorption volume above the relative pressure of 0.8. The specific surface area of the composite from BET analysis was found to be 27.38 $m^2 g^{-1}$. The Barrett–Joiner–Halenda (BJH) method was used to calculate the pore size on the desorption branch of the $N_2$ adsorption–desorption isotherm. The pore volume *versus* pore diameter curve (Fig. S4b†) shows a sharp peak at 3.7 nm along with a broad distribution of mesopores. This behaviour also confirms the predominance of mesopores in $G–Fe_3O_4$.[28]

## Adsorption parameters

To further explore the adsorption property of the prepared materials, a batch adsorption experiment was conducted; the corresponding adsorption parameters of lead ions onto $G–Fe_3O_4$ nanocomposites are shown in Fig. S5.† Fig. S5a† shows the removal efficiency of lead ions onto $G–Fe_3O_4$ surfaces, as a function of contact time. It was noted that the adsorption of Pb increased quickly with an increase in contact time, and at a certain period it reached an equilibrium state. It was seen that adsorption is rapid due to the availability of numerous active sites on the adsorbent surface at the initial stage. This fast adsorption may be due to the special one-atom-thick layered structure of GO. In addition, because it contacts Pb ions in the aqueous solution, adsorption occurs immediately due to higher driving force to enable the faster transfer of Pb ions to the active sites on the surface of $G–Fe_3O_4$. With further increase in time, the diminishing availability of the remaining active sites and decrease in the driving force makes the adsorption process slow, and thus equilibrium is achieved much later. Thus, the adsorption rate decreases. The equilibrium time increases with increasing initial Pb ion concentration. It can be concluded from Fig. S5a† that it took about 100 min to reach adsorption equilibrium. From 120–180 min, the concentration of the ions remained unchanged.

Fig. S5b† shows the amount of adsorbed ions as a function of the initial concentration from aqueous solution. The initial concentration provides an important driving force to overcome the mass transfer of Pb ions between the aqueous and solid phases; hence, a higher initial concentration of Pb ions may increase adsorption capacity. In this experiment, the following concentrations (10, 20, 30, 40, 50 and 60 mg $L^{-1}$) were chosen at pH 5, equilibrium time of 120 min and $T = 310$ K. With an increase in ion concentration, the percentage of ion adsorption increased. About 99% of the Pb ions were adsorbed onto $G–$
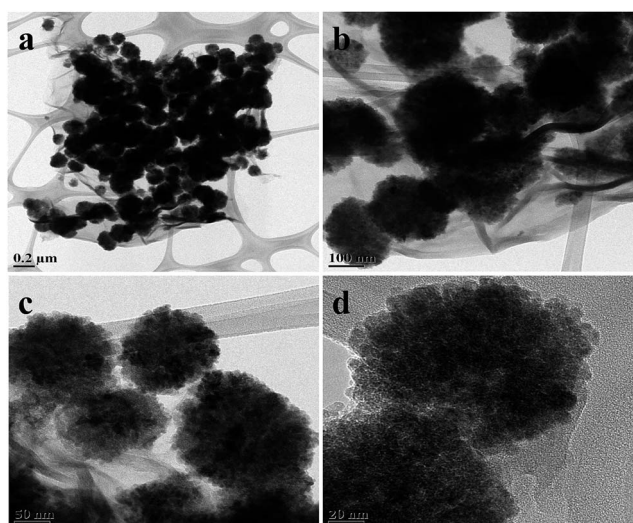


Fig. 1   TEM images of G–Fe$_3$O$_4$ nanocomposites.

Fe$_3$O$_4$ surface after 120 min for an initial Pb concentration of 50 mg L$^{-1}$. Fig. S5c† shows the variation of adsorption capacity of Pb ions by G–Fe$_3$O$_4$ at various pH values. The adsorption capacity increases with an initial pH of 3 and reaches a maximum at pH 7. The effect of pH on the adsorption percentage of Pb ions on the adsorbent G–Fe$_3$O$_4$ were studied at varying pH values over the range of 3–8 using the same concentration of ions; the results are displayed in Fig. S5c.† Although a maximum uptake was noted at pH 8, as the pH increased more than 7, the metal ion started to precipitate. Therefore, no experiment was conducted at pH > 7. The increase in adsorption capacity at pH > 7 could be attributed to both the adsorption of ions onto the surface of adsorbent and precipitation. Therefore, the optimal pH was observed to be 5 for the adsorption of Pb ions. By further increasing the pH adsorption decreased, which was probably due to the formation of Pb hydroxides and chemical precipitation.

Fig. S5d† shows the adsorption% of Pb ions onto G–Fe$_3$O$_4$ matrix as a function of temperature. The percentage-adsorption experiments were conducted at 300, 310 and 320 K to investigate the effect of temperature with an initial concentration of Pb ions of 20 mg L$^{-1}$, adsorbents dosage of 25 mg L$^{-1}$ and pH 5. When temperature was increased from 300 to 320 K, the percentage of adsorption of Pb ions increased from 85.2% to 87.2%. An increase in the amount of equilibrium adsorption of Pb ions with an increase in temperature may be explained by the fact that the adsorbent sites were more active at higher temperatures. This condition shows that adsorption occurs more as a physical rather than a chemical process.

## Adsorption isotherm study

Developing an appropriate isotherm model for adsorption is essential to design and optimize an adsorption process. Several isotherm models have been developed for evaluating the equilibrium adsorption of compounds from solutions such as Langmuir,[29,30] Fruendlich and Dubinin-Radushkevich. The experimental results of this study were fitted with two models. The equilibrium adsorption isotherms are important for determining the adsorption capacity of Pb ions and diagnose the nature of adsorption onto G–Fe$_3$O$_4$ surface.[31]

The equilibrium concentration adsorption capacity of adsorbent was calculated as:

$$q_e = \frac{v(C_0 - C_e)}{w} \tag{2}$$

where $q_e$ is the equilibrium adsorption capacity of adsorbent in mg metal per g adsorbent, $C_0$ is the initial concentration of the metal ions in mg L$^{-1}$, $C_e$ is the equilibrium concentration of the metal ions in mg L$^{-1}$, $v$ is the volume of metal ion solution in L, and $w$ is the weight of adsorbent in g.

The adsorption data can then be correlated with Langmuir and Freundlich isotherm model equations. In this study, two classical adsorption models were employed to describe the ion adsorption equilibrium. The Langmuir isotherm is valid for monolayer adsorption onto a surface with a finite number of identical sites.

The Langmuir and Freundlich adsorption isotherm models can be expressed as follows:

$$\frac{C_e}{q_e} = \frac{1}{K_d q_m} + \frac{1}{q_m} C_e \tag{3}$$

$$\ln q_e = \ln K_F + \frac{1}{n} \ln C_e \tag{4}$$

where $C_e$ (mg L$^{-1}$) is the equilibrium concentration of ion in the solution, $q_e$ and $q_m$ (mg g$^{-1}$) are the maximum adsorption capacity at equilibrium, and $K_d$ (L mg$^{-1}$) is the effective dissociation constant that relates to the affinity binding site, $K_F$ and $n$ are physical constants representing the adsorption capacity and intensity of adsorption, respectively.

The slope and intercept of the linear Freundlich equation are $1/n$ and $\ln K_F$, respectively. Fig. 2 shows the adsorption isotherm of Pb ions onto G–Fe$_3$O$_4$ surfaces at 300 K, 310 K and 320 K. From the graph, it can be seen that the adsorption capacity increased with an increase in temperature, indicating an endothermic reaction. We observed that the adsorption percentage increased along with an increase in $C_e$.

Two models, the Langmuir and Freundlich isotherm models, have been adopted for Pb ion adsorption onto G–Fe$_3$O$_4$ at different temperatures and at different pH values in the experiment. The relative parameters were calculated from the equation and are listed in Table 1. It can be seen from the $R^2$ values that the adsorption isotherms can be simulated well by the two models. The Table suggests that the adsorption of Pb on G–Fe$_3$O$_4$ is mainly a monolayer type.

It can be inferred from the $R^2$ values given in Table 1 that the Langmuir isotherm fits the experimental data better than the Freundlich isotherm. It was also noted that adsorption is a
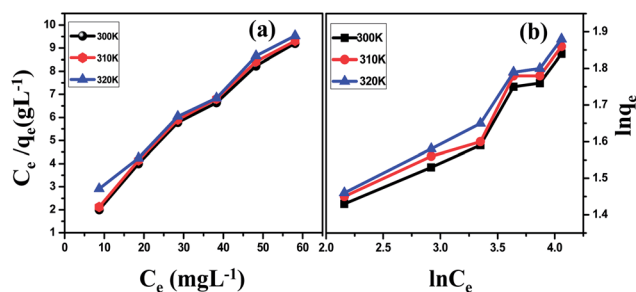


Fig. 2 Percentage of adsorption isotherm of Pb ions onto G–Fe$_3$O$_4$ surfaces: (a) Langmuir isotherm; (b) Freundlich isotherm. Initial concentration of the ion was 10, 20, 30, 40, 50, and 60 mg L$^{-1}$; pH 5; contact time, 120 min and adsorbent dosage 25 mg L$^{-1}$.

Table 1   Isotherm models for the adsorption of Pb ions onto G–Fe$_3$O$_4$

| Temp (K) | Langmuir | | | Freundlich | | |
|---|---|---|---|---|---|---|
| | $K_d$ | $q_m$ (mg g$^{-1}$) | $R^2$ | $K_F$ | $n$ | $R^2$ |
| 300 | 0.12 | 69 | 0.998 | 4.2 | 0.23 | 0.9328 |
| 310 | 0.1 | 69 | 0.992 | 26.96 | 0.24 | 0.9248 |
| 320 | 0.1 | 67 | 0.9818 | 10.86 | 0.27 | 0.9686 |

monolayer process and that the adsorption of all species requires equal activation energy. From the table it is clear that at different temperatures there is change in $q_m$ and $K_d$ values; the maximum adsorption capacity $q_m$ obtained was 69 mg g$^{-1}$.

## Thermodynamic parameters

Thermodynamic parameters provide additional in-depth information regarding the inherent energetic changes involved during adsorption. To assess thermodynamic parameters, the adsorption isotherm of Pb ions onto G–Fe$_3$O$_4$ surfaces were measured at 300, 310 and 320 K, and the changes in thermodynamic parameters of standard Gibbs free energy of adsorption ($\Delta G^\circ$), standard enthalpy ($\Delta H^\circ$) and standard entropy ($\Delta S^\circ$) were calculated from the variation of thermodynamic equilibrium constant, $K_o$, with a change in temperature.

The standard Gibbs free energy of adsorption, $\Delta G^\circ$, is

$$\Delta G^\circ = -RT \ln K_o \qquad (5)$$

where $R$ = gas constant, $T$ = absolute temperature

$$RT \ln K_o = T\Delta S^\circ - \Delta H^\circ \qquad (6)$$

From Table 2, it is clear that the value of change in standard enthalpy is positive and Gibbs free energy is negative, showing that the adsorption of Pb ions onto G–Fe$_3$O$_4$ adsorbents is endothermic. Consequently, it can be seen that there is a change in the adsorption as temperature increases, and here it is seen that the adsorption is same at 300 and 310 K.

A positive standard enthalpy change suggests that the interaction of Pb ions with G–Fe$_3$O$_4$ is endothermic, which is supported by the increasing adsorption of Pb with increase in temperature. A comparison has been made of the adsorption capacity for various adsorbents cited in the literature for the removal of Pb ions (Table 3). It is clear from the table that our

G–Fe$_3$O$_4$-based adsorbent has the maximum Pb ion adsorption capability.

## Photo-Fenton degradation of dye

Further work was carried out for probing the role of this material towards dye degradation applications. Dye adsorption on the catalyst surface is a prerequisite for efficient dye removal. The adsorption of methylene blue dye was studied within a 30 min time interval using UV-vis spectroscopy. Fig. S6† shows that the adsorption of dye is quite rapid in the first 30 min, and then gradually rises with increase in adsorption time. After 180 min, the amount of dye removed from the suspension is calculated using the following equation:

$$\text{Removal (\%)} = \frac{1 - C_t}{C_0} \times 100 \qquad (7)$$

where $C_0$ (mg L$^{-1}$) is the initial dye concentration before removal and $C_t$ (mg L$^{-1}$) is the concentration of dye remaining in the solution after stirring for 180 min in the dark. The removal efficiency of the composite at different concentrations (0.1 to 0.3 g L$^{-1}$) and graphene is 49.6, 79.6, 98.5 and 99%.

Graphene shows much better removal efficiency compared with the composite of the same amount (0.2 g L$^{-1}$), which can be attributed to the large surface area of graphene sheets. In addition, π–π stacking between the dyes and π-conjugated regions of the sheets can offer more active adsorption sites and catalytic reaction centers.[36] The photocatalytic property of the composite is measured by the degradation of the dye in the presence of visible light (Fig. 3). Before light irradiation, the suspension of the catalyst and the dye was stirred for 180 min in the dark to reach the adsorption–desorption equilibrium between the catalyst and the dye. It has been observed from Fig. 3(a and c) that upon the addition of H$_2$O$_2$ in the presence of visible light, the degradation rate increases rapidly. For comparison, the effect of H$_2$O$_2$ in the dark on G–Fe$_3$O$_4$ composite is also shown in a graph (Fig. 3(b)); an enlarged view of dye degradation is also shown as an inset in Fig. 3. The enhancement in dye degradation can be attributed to the synergistic interaction between GO and Fe$_3$O$_4$ nanoparticles. The electron transfer between NPs and GO sheet facilitates the
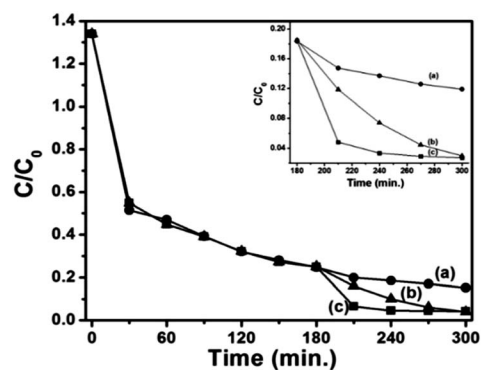
**Table 2** Thermodynamics parameters of Pb ion onto G–Fe$_3$O$_4$

| Temp (K) | $\Delta G^\circ$ | $\Delta H^\circ$ (kJ mol$^{-1}$) | $\Delta S^\circ$ (kJ mol$^{-1}$) |
|---|---|---|---|
| 300 | −1643 | | |
| 310 | −4796 | 255.8 | 15.908 |
| 320 | −9686 | | |

**Table 3** Comparison of adsorption capacities of various adsorbents

| Adsorbent | $q_m$ (mg g$^{-1}$) | pH | Ref. |
|---|---|---|---|
| CNTs (HNO$_3$) | 35.60 | 5 | 32 |
| Granular activated carbon | 15.58 | 5 | 33 |
| Powdered activated carbon | 26.90 | 5 | 33 |
| Microbead | 16.4 | 5 | 34 |
| Iron coated sand | 1.21 | 5 | 35 |
| G–Fe$_3$O$_4$ | 69 | 5 | Present work |



**Fig. 3** Photo-Fenton degradation spectra of G–Fe$_3$O$_4$ composite at a concentration of 0.2 g L$^{-1}$ in the presence of (a) visible light, (b) H$_2$O$_2$ and (c) visible light and H$_2$O$_2$. (Inset shows the expanded view).

reduction of $Fe^{3+}$ to $Fe^{2+}$ ion. Subsequently, $Fe^{2+}$ would react with $H_2O_2$ to produce hydroxyl radicals ($OH^{\cdot}$). The hydroxyl radicals produced as a result of Fenton/photo-Fenton processes attacks the dye adsorbed on the surface of the catalyst and degrade it to $CO_2$ and $H_2O$.[37,38]

For the recycling of G–$Fe_3O_4$ composite, the absorbent was separated, washed and then reused. The recycled adsorbed behaviour is shown in Fig. S7.† It was observed that the removal efficiency of the dye was over 95% up to 5 cycles. The photocatalytic activity of the recycled catalyst was also investigated, and the results are shown in Fig. S7.† There was no noticeable change in the photocatalytic activity of the recycled catalyst after five cycles under visible light irradiation, indicating that the magnetically separable photocatalyst is stable and effective for the degradation of organic pollutants in water.

## Antibacterial activity of G -$Fe_3O_4$

Fig. 4 shows that about 22.66% of the cells were only viable when treated with G–$Fe_3O_4$, whereas with graphene about 65.33% of the cells were viable. The two activities were further examined, *i.e.*, concentration and time-dependent behaviour of G–$Fe_3O_4$ on *E. coli* cells. Different concentrations of G–$Fe_3O_4$ (0, 25, 50, 100, 200 ppm) dispersions were incubated with *E. coli* cells for 60 min and then plated for investigating cell viability. Only *E. coli* cells and graphene were controls.

It was observed that 25 ppm G–$Fe_3O_4$ could inhibit 43% of the cells because the recorded cell viability according to Fig. S8(a)† is 57%. In addition, 100 ppm was sufficient to inhibit bacteria for cell viability at 26.84% *E. coli* cells.

On the other hand, in a time-dependent study, we observed that when 100 ppm of G–$Fe_3O_4$ dispersion was treated with *E. coli* cells for various time intervals from 0 to 90 min, 60 min was sufficient to kill bacteria, showing 23.74% cell viability (Fig. S8(b)†). The loss of *E. coli* viability progressively decreased with an increase in G–$Fe_3O_4$ concentration. *E. coli* viability almost decreased from 57% by 25 ppm G–$Fe_3O_4$ to 21% with 200 ppm.

The majority of *E. coli* cells were killed after incubation with G–$Fe_3O_4$ at a concentration of 100 ppm. In a similar manner, cell viability w.r.t. time from 0–90 min drastically reduced from 64.66% to 19.66%.
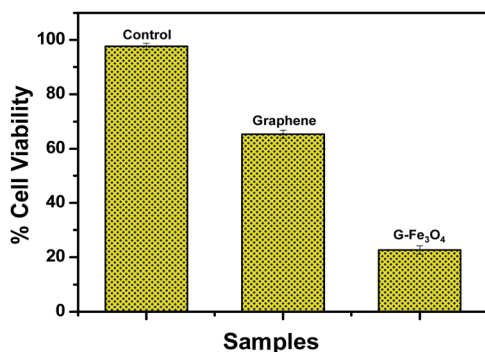


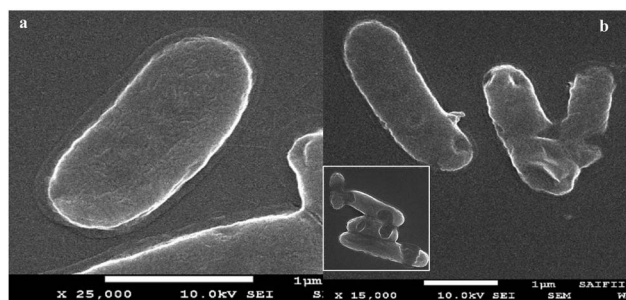Fig. 4 Cell viability of *E. coli* when treated with graphene and G–$Fe_3O_4$.



Fig. 5 (a) FE-SEM images of *E. coli* cells control and (b) rupture by G–$Fe_3O_4$.

## Destruction of bacterial membrane

FE-SEM was used to illustrate the interaction between G–$Fe_3O_4$ and *E. coli*. In Fig. 5(a), *E. coli* cells as a control show the entire cell wall without any rupture, whereas Fig. 5(b) shows complete disintegration of the cell wall. Spikes created on the *E. coli* cells are a clear indication that G–$Fe_3O_4$ interacted with the cell wall. This kind of cell wall rupture is irreversible damage induced by direct contact with G–$Fe_3O_4$.

Fig. S9† shows the biocompatibility study. It was essential to understand whether G–$Fe_3O_4$, if leached during water purification, would cause harm to normal cells. As shown, graphene has less cell compatibility of about 54.11% in 2 mg $mL^{-1}$, whereas at the same concentration compatibility for G–$Fe_3O_4$ is about 92.99%. Presence of $Fe_3O_4$, which supposedly is biocompatible, has been a good support with graphene as a biocompatible material.

## Biochemical assay of total cellular protein degradation due to G -$Fe_3O_4$

Degradation of protein due to the effect of graphene and G–$Fe_3O_4$ was performed by Folin-Lowry test. Table 4 (in ESI†) also indicates a reduction in protein content when *E. coli* was treated with graphene and G–$Fe_3O_4$ individually. The reduction in total protein content was found to be approximately 86.66% in the case of G–$Fe_3O_4$. The total cellular protein degraded drastically to 86.66 when treated with G–$Fe_3O_4$, as observed from Table 2, whereas the control showed about 236% of protein. Perhaps this is why only 22.66% of the *E. coli* could survive (*i.e.*, 78% mortality) when exposed to 100 ppm G–$Fe_3O_4$ nanocomposite, suggesting that microbial death is due to the degradation of total cellular protein.

## Total protein assay (by SDS-PAGE methods) of *E. coli* due to G-$Fe_3O_4$

Fig. 6 depicts the degradation of protein as analyzed by SDS-PAGE electrophoresis upon treating *E. coli* cells with G–$Fe_3O_4$. It is clear from the protein degradation results that stress-mediated protein degradation of cell membrane left only one higher density protein intact, whereas the rest of the proteins were denatured, unlike proteins treated with graphene alone or control.
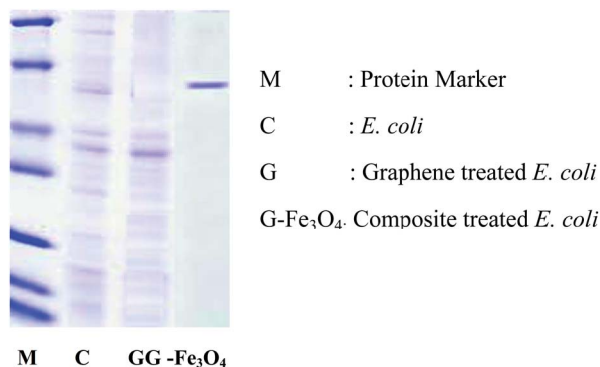
M     : Protein Marker

C     : *E. coli*

G     : Graphene treated *E. coli*

G-Fe₃O₄: Composite treated *E. coli*

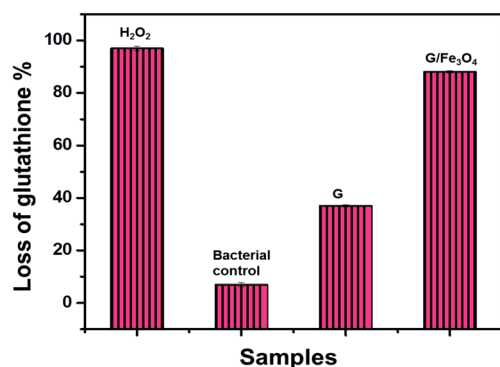**Fig. 6** Protein degradation by G–Fe₃O₄.



**Fig. 7** Oxidative stress release by *E. coli* due to G–Fe₃O₄.

## Glutathione oxidation due to G -Fe₃O₄ treatment

Disregulation of $H_2O_2$ pathway in a cellular membrane causes oxidative stress. To examine oxidative stress, *in vitro* GSH oxidation was mediated.

GSH is a tripeptide with thiol groups, and is an antioxidant in bacteria at a concentration ranging between 0.1 and 10 mM. GSH can prevent damages to cellular components caused by oxidative stress. Thiol groups (–SH) in GSH can be oxidized to disulfide bonds (–S–S–), which converts GSH to glutathione disulfide. GSH has been used as an oxidative stress indicator in cells. The Ellman's assay is able to quantify the concentration of thiol groups in GSH. When 0.4 mM GSH was incubated with 100 ppm G–Fe₃O₄, the oxidation of GSH gradually advanced, extending the reaction time by up to 60 min. Fig. 7 shows that the fraction of GSH oxidized by G–Fe₃O₄ increases in comparison with graphene. Comparably, G–Fe₃O₄ has significantly higher oxidation reactivity up to 89.32% more than graphene at the same reaction time and concentration of 60 min in 125 μg mL⁻¹ of G–Fe₃O₄. The oxidation of GSH indirectly confirms that G–Fe₃O₄ is capable of mediating ROS-independent oxidative stress toward bacterial cells.

Thus, the prepared composite is effective for multipurpose applications due to the combined advantages of Fe₃O₄ and graphene.

## Conclusions

G–Fe₃O₄ was synthesized by a simple one-step solvothermal route from graphene oxide and iron oxide nanoparticles. This nanostructure serves as an efficient adsorbent for the removal of heavy metal ions from waste water. The maximum adsorption capacity of G–Fe₃O₄ was 17 mg g⁻¹ at an initial Pb concentration of 20 mg L⁻¹ and temperature of 310 K, indicating that G–Fe₃O₄ is effective for the adsorption of Pb(II) ions. The experimental data fitted well with the Langmuir isotherm model. The monolayer adsorption capacity of Pb by G–Fe₃O₄ was found to be 69 mg g⁻¹ at 310 K at pH 5. Thermodynamic investigations indicated that the adsorption reaction was spontaneous and endothermic. Results indicate that such materials could be used as adsorbents for the removal of heavy metal ions. Photodegradation of methylene blue dye was successfully achieved up to 5 cycles. Antibacterial activity depicts that only 22.33% of the cells were viable when treated with G–Fe₃O₄. Further protein degradation confirmed that a higher molecular weight protein was not denatured, whereas the rest of the proteins as compared with *E. coli* had disintegrated. This was due to the release of some ROS and disintegration of disulphide bonds.

## Acknowledgements

## References

1 A. K. De, *Environmental Chemistry*, Wiley Eastern Ltd., New Delhi, 2nd edition, 1992.
2 S. Singh, K. C. Barick and D. Bahadur, *J. Hazard. Mater.*, 2011, **193**(3), 1539–1547.
3 N. A. Babarinde, J. O. Babalola and R. A. Sanni, *Int. J. Phy. Sci.*, 2006, **1**, 23–26.
4 A. Saeed, M. Iqbal and M. W. Akhtar, *J. Hazard. Mater. B*, 2005, **117**, 65–73.
5 T. A. Davis, B. Volesky and A. Mucci, *Water Res.*, 2003, **37**, 4311–4330.
6 G. McKay and Y. S. Ho, *Water Res.*, 1999, **33**, 578–584.
7 B. H. Hameed, A. A. Ahmad and N. Aziz, *Desalination*, 2009, **247**, 551–560.
8 V. K. Gupta, A. Mittal, R. Jain, M. Mathur and S. Sikarwar, *J. Colloid Interface Sci.*, 2006, **303**, 80–86.
9 S. Liu, T. Helen Zeng, M. Hofmann, E. Burcombe, J. Wei, R. Jiang, J. Kong and Y. Chen, *ACS Nano*, 2011, **5**(9), 6971–6980.
10 S. Singh, K. C. Barick and D. Bahadur, *Nanomater. Nanotechnol.*, 2013, **3**, 1–19.
11 M. J. Allen, V. C. Tung and R. B. Kaner, *Chem. Rev.*, 2010, **110**, 132–145.
12 M. Ghaedi, A. Hassanzadeh and S. N. Kokhdan, *J. Chem. Eng. Data*, 2011, **56**, 2511–2520.

13 T. S. Sreeprasad, S. M. Maliyekkal, K. P. Lisha and T. Pradeep, *J. Hazard. Mater.*, 2011, **186**, 921–931.

14 J. Xu, L. Wang and Y. Zhu, *Langmuir*, 2012, **28**, 8418–8425.

15 S. Gupta, T. S. Sreeprasad, S. M. Maliyekkal, S. K. Das and T. Pradeep, *ACS Appl. Mater. Interfaces*, 2012, **4**, 4156–4163.

16 S. Wang, H. Sun, H. M. Ang and M. O. Tade, *Chem. –Eng. J.*, 2013, **226**, 336–347.

17 M. Machida, T. Mochimaru and H. Tatsumoto, *Carbon*, 2006, **44**, 2681–2688.

18 R. Zacharia, H. Ulbricht and T. Hertel, *Phys. Rev. B: Condens. Matter Mater. Phys.*, 2004, **69**, 55406.

19 Z. Wu, D. Wang, W. Ren, J. Zhao, G. Zhou, F. Li and H. Cheng, *Adv. Funct. Mater.*, 2010, **20**, 3595–3602.

20 J. Hu, L. Zhong, W. Song and L. Wan, *Adv. Mater.*, 2008, **20**, 2977–2982.

21 Y. M. Zhai, J. F. Zhai, M. Zhou and S. J. Dong, *J. Mater. Chem.*, 2009, **19**, 7030–7035.

22 S. Liu, T. H. Zeng, M. Hofmann, E. Burcombe, J. Wei, R. Jiang, J. Kong and Y. Chen, *ACS Nano*, 2011, **5**, 6971–6980.

23 W. S. Hummers and R. E. Offeman, *J. Am. Chem. Soc.*, 1958, **80**, 1339.

24 J. P. Ruparelia, S. P. Duttagupta, A. K. Chatterjee and S. Mukherji, *Desalination*, 2008, **232**, 145–156.

25 B. Li, Y. Fu, H. Xia and X. Wang, *Mat. Lett.*, 2014, **122**, 193–196.

26 Z. S. Wu, W. Ren, L. Wen, L. Gao, J. Zhao, Z. Chen, G. Zhou, F. Li and H. M. Cheng, *ACS Nano*, 2010, **4**, 3187–3194.

27 J. K. Lim, S. P. Yeap, H. X. Che and S. C. Low, *Nanoscale Res. Lett.*, 2013, **8**, 381.

28 K. C. Barick, S. Singh, M. Aslam and D. Bahadur, *Microporous Mesoporous Mater.*, 2010, **134**, 195–202.

29 H. Y. Koo, H. J. Lee, H. A. Go, Y. B. Lee, T. S. Bae, J. K. Kim and W. S. Choi, *Chem.–Eur. J*, 2011, **17**, 1214–1219.

30 L. Ren, S. Huang, W. Fan and T. Liu, *Appl. Surf. Sci.*, 2011, **258**, 1132–1138.

31 T. Liu, Y. Li, Q. Du, J. Sun, Y. Jiao, G. Yang, Z. Wang, Y. Xia, W. Zhang, K. Wang, H. Zhu and D. Wu, *Colloids Surf., B*, 2012, **90**, 197–203.

32 Y. H. Li, Z. Di, J. Ding, D. Wu, Z. Luan and Y. Zhu, *Water Res.*, 2005, **39**, 605–609.

33 Z. Reddad, C. Gerente, Y. Andres and P. Cloirec Le, *Environ. Sci. Technol.*, 2002, **36**, 2067–2073.

34 B. Salih, A. Denizli, C. Kavakli, R. Say and E. Piskin, *Talanta*, 1998, **77**, 1147–1154.

35 C. H. Lai and C. Y. Chen, *Chemosphere*, 2001, **44**, 1177–1184.

36 H. Zhang, X. Lv, Y. Li, Y. Wang and J. Li, *ACS Nano*, 2010, **4**, 380.

37 S. Q. Liu, B. Xiao, L. R. Feng, S. S. Zhou, Z. G. Chen, C. B. Liu, F. Chen, Z. Y. Wu, N. Xu, W. C. Oh and Z. D. Meng, *Carbon*, 2013, **64**, 197–206.

38 S. Guo, G. Zhang, Y. Guo and J. C. Yu, *Carbon*, 2013, **60**, 437–444.